Molecular motor tug-of-war regulates elongasome cell wall synthesis dynamics in *Bacillus subtilis*

Stuart Middlemiss[1*], Matthieu Blandenet[1], David M Roberts[2], Andrew McMahon[2], James Grimshaw[1], Joshua M Edwards [2,1], Zikai Sun[3], Kevin D Whitley[1], Thierry Blu[3], Henrik Strahl[1], and Séamus Holden[2,1*]

1: Centre for Bacterial Cell Biology, Biosciences Institute, Faculty of Medical Sciences, Newcastle University, Newcastle upon Tyne, UK;

2: School of Life Sciences, University of Warwick, Gibbet Hill Campus, Coventry, UK.

3: Department of Electronic Engineering, The Chinese University of Hong Kong, Hong Kong.

*:Corresponding authors: seamus.holden@warwick.ac.uk, stuart.middlemiss@newcastle.ac.uk, h.strahl@newcastle.ac.uk

ABSTRACT

Most rod-shaped bacteria elongate by inserting new cell wall material into the inner surface of the cell sidewall. This is performed by class A penicillin binding proteins (PBPs) and a highly conserved protein complex, the elongasome, which moves processively around the cell circumference and inserts long glycan strands that act as barrel-hoop-like reinforcing structures, thereby giving rise to a rod-shaped cell. However, it remains unclear how elongasome synthesis dynamics and termination events are regulated to determine the length of these critical cell-reinforcing structures. To address this, we developed a method to track individual elongasome complexes around the entire circumference of *Bacillus subtilis* cells for minutes-long periods using single molecule fluorescence microscopy. We found that the *B. subtilis* elongasome is highly processive and that processive synthesis events are frequently terminated by rapid reversal or extended pauses. We found that cellular levels of RodA regulate elongasome processivity, reversal and pausing. Our single molecule data, together with stochastic simulations, show that elongasome dynamics and processivity are regulated by molecular motor tug-of-war competition between several, likely two, oppositely oriented peptidoglycan synthesis complexes associated with the MreB filament. Our data, thus, demonstrate that molecular motor tug-of-war is a key regulator of elongasome dynamics in *B. subtilis*, which likely also regulates the cell shape via modulation of elongasome processivity.

INTRODUCTION

Almost all bacteria are encased by a peptidoglycan-based cell wall, which is essential for their survival. To maintain a robust cell wall during growth and division, bacterial cell wall synthesis proteins must accurately and reliably expand and remodel a precisely shaped structure more than 100 times their size. Due to the high internal turgor of a bacterial cell, major errors in cell wall synthesis trigger lethal cell lysis. For this reason, the cell wall synthesis machinery is the principal target of many first-line antibiotics such as β-lactams, as well as last resort antibiotics such as vancomycin and daptomycin that are used to treat infections caused by multidrug resistant pathogens. A better understanding of the biophysical principles of cell wall synthesis is therefore critical for deciphering how this highly successful class of antibiotics can induce bacterial cell death, for developing the next generation of cell-wall-targeting antibiotics, as well as developing countermeasures against the adaptive processes bacteria utilise to evade those already in clinical use.

Most rod-shaped bacteria, including key model organisms such as Gram-positive *B. subtilis* and Gram-negative *Escherichia. coli*, elongate by inserting new cell wall material into the inner surface of the cell wall. This is performed by class A penicillin binding proteins (PBPs) and a highly conserved protein complex, the elongasome, which inserts long peptidoglycan strands circumferentially around the cell, giving rise to a rod-shaped cell morphology [1,2].

Gram-positive rod-shaped bacteria such as *B. subtilis* have a single cytoplasmic membrane surrounded by a thick multi-layered peptidoglycan cell wall. Elongasome-driven cell wall synthesis is performed by a coordinated action of two enzymes: the glycosyltransferase RodA, which polymerizes glycan strands, and a cognate class B transpeptidase (PBP2A or PBPH in *B. subtilis*), which attaches new strands to the existing cell wall [3]. These proteins, together with additional regulatory factors, are associated with the actin-homolog MreB, which forms antiparallel double-filament structures [4]. Each double filament is around 170 nm long [5] and monomers are around 5 nm long [4], suggesting that the average MreB double filament consists of around 68 subunits. These cytoskeletal structures guide peptidoglycan insertion perpendicular to the long axis of the cell [6]. *B. subtilis* also encodes two functionally redundant MreB homologues, Mbl and MreBH, which copolymerize with MreB [7]. As continuous glycan chains can stretch less than cross-linked peptides, circumferentially oriented glycan strands reinforce the cell sidewall and thereby establish a rod-like cell shape [1,2]. The overall level of elongasome-driven cell wall synthesis plays a major role in establishing both the all overall rod shape morphology and the specific cell diameter. Hereby high levels of elongasome-driven cell wall synthesis lead to stiff, narrow, rod-shaped cells whereas low levels lead to soft, wide, spherical cells [1,2].

The processive motion of the elongasome is driven by peptidoglycan synthesis [8–10]. It is likely that the initial length of elongasome-synthesized glycan strands is determined by the processivity of the elongasome, i.e., the distance around the cell circumference that elongasome moves in one direction without interruption. This should reflect an individual processive synthesis event. As the primary function of the elongasome is to maintain rod-shape and elongate the cell sidewall by inserting circumferential glycan strands, we hypothesized that elongasome processivity, and thus the length of elongasome-synthesized glycan strands, is likely to have substantial effect on cell wall stiffness and thereby cell shape. Put simply – if elongasome synthesized glycans act as reinforcing structures similar to metal hoops around a wooden barrel, the length of those reinforcing structures should determine the stiffness of the cell's short axis.

To test these hypotheses, we developed a new method to track individual elongasome complexes around the entire cell circumference for minutes-long periods. We found that the *B. subtilis* elongasome is highly processive and exhibits frequent reverses and pauses. Intriguingly, we found that cellular levels of RodA regulate elongasome processivity, reversal and pausing. Together with

stochastic simulations, our single molecule data support an end-binding tug-of-war model where competition between two opposing peptidoglycan synthesis complexes, bound to each end of the symmetrical MreB double filament, determine elongasome dynamics and processivity. Elongasome tug-of-war may also regulate *B. subtilis* cell shape via modulation of elongasome processivity. Our data demonstrate that molecular motor tug-of-war is a key regulator of elongasome dynamics, which may also play a major role in bacterial cell shape control in *B. subtilis.*

RESULTS

The *B. subtilis* elongasome is highly processive and frequently reverses and pauses

Previously, it was only possible to track elongasomes that are performing cell wall synthesis over distances less than about 500 nm, owing to the geometrical limitations of total internal reflection fluorescence (TIRF) imaging, which is usually used for such measurements but which only illuminates a small fraction of the cell circumference [18, 19]. Previous estimates of elongasome processivity have been in the range of 400-600 nm [11], suggesting that these measurements were limited by the shallow illumination depth of the technique. We define processivity as the distance travelled in a continuous motion by an elongasome around the circumference of the cell until pausing, reversal or another terminating event. In a kymograph, this corresponds to the displacement of signal around the cell circumference over time (Supplementary Figure 2).

To address this limitation, we combined single molecule tracking with VerCINI (vertical cell imaging by nanostructured immobilization), a method we developed to orient rod-shaped cells perpendicular to the microscope imaging plane [12]. We used single molecule VerCINI (smVerCINI) to focus on a slice of the bacterial cell sidewall approximately 0.5 µm thick (determined by the microscope objective depth of field), and tracked individual membrane bound MreB molecules in live *B. subtilis* cells using a previously characterized functional, native-locus MreB-HaloTag fusion [6] (Supplementary Figure 1). We used a sub-stoichiometric labelling concentration of the bright cell-permeable HaloTag ligand JF549 (a JaneliaFluor dye [13]) to sparsely label individual MreB molecules within membrane-bound MreB filaments (Fig. 1a). Because MreB motion is circumferential [5,6], MreB filament dynamics are mostly constrained to within the VerCINI focal plane, allowing long term imaging of MreB filament dynamics (Fig. 1a).

We tracked MreB molecules using long (500 ms) camera exposure times such that freely diffusive molecules were not detected, allowing us to exclusively analyse MreB molecules assembled within membrane bound MreB filaments, while simultaneously reducing effective photobleaching rate using long (6 s) strobe intervals. We analysed the data using kymographs (see schematic Supplementary Figure 2, also definitions SI Table 1). We found that MreB filaments remain assembled at the membrane for extended periods of time, frequently reverse direction and sometimes pause for extended periods (Fig. 1b-c, Supplementary Videos 1-4). As MreB filament motion is dependent on peptidoglycan synthesis, motile MreB filaments should correspond to fully assembled elongasome complexes actively engaged in peptidoglycan synthesis. Paused MreB filaments could correspond either to filaments in which some or all the other critical elongasome components are missing/ unbound, or to fully assembled complexes currently not engaged in peptidoglycan synthesis.

We determined the binding lifetime of MreB subunits within filaments and the JF549 photobleaching lifetime using the stroboscopic illumination method of Gebhardt and coworkers [14]. We measured the apparent binding lifetime of MreB molecules by single molecule tracking and systematically increased the total time interval between frames (strobe interval), while keeping the exposure time and thus total light dose constant (Fig. 1d-e). As the strobe interval increased, the fraction of time for which the molecule was illuminated decreased thus increasing the effective photobleaching lifetime.

This not only allows molecules to be tracked for longer but also allows accurate determination of both molecule binding lifetime time and dye photobleaching lifetime by fitting an equation describing the relationship between those quantities, the strobe interval, and the apparent binding lifetime (Fig. 1e, Methods).

We measured the MreB binding lifetime as 128 s [95% CI: 109, 164] showing that the MreB filaments remain assembled at the membrane for extended periods of time. This measurement represents a lower bound on the lifetime of both assembled MreB filaments, as it likely represents a combination of MreB filament unbinding from the membrane, dissociation of MreB subunits from the MreB filament and occasional migration of the elongasome complexes beyond the microscope depth of field. We also measured the JF549 bleaching lifetime as 13s [95% CI: 11, 16].

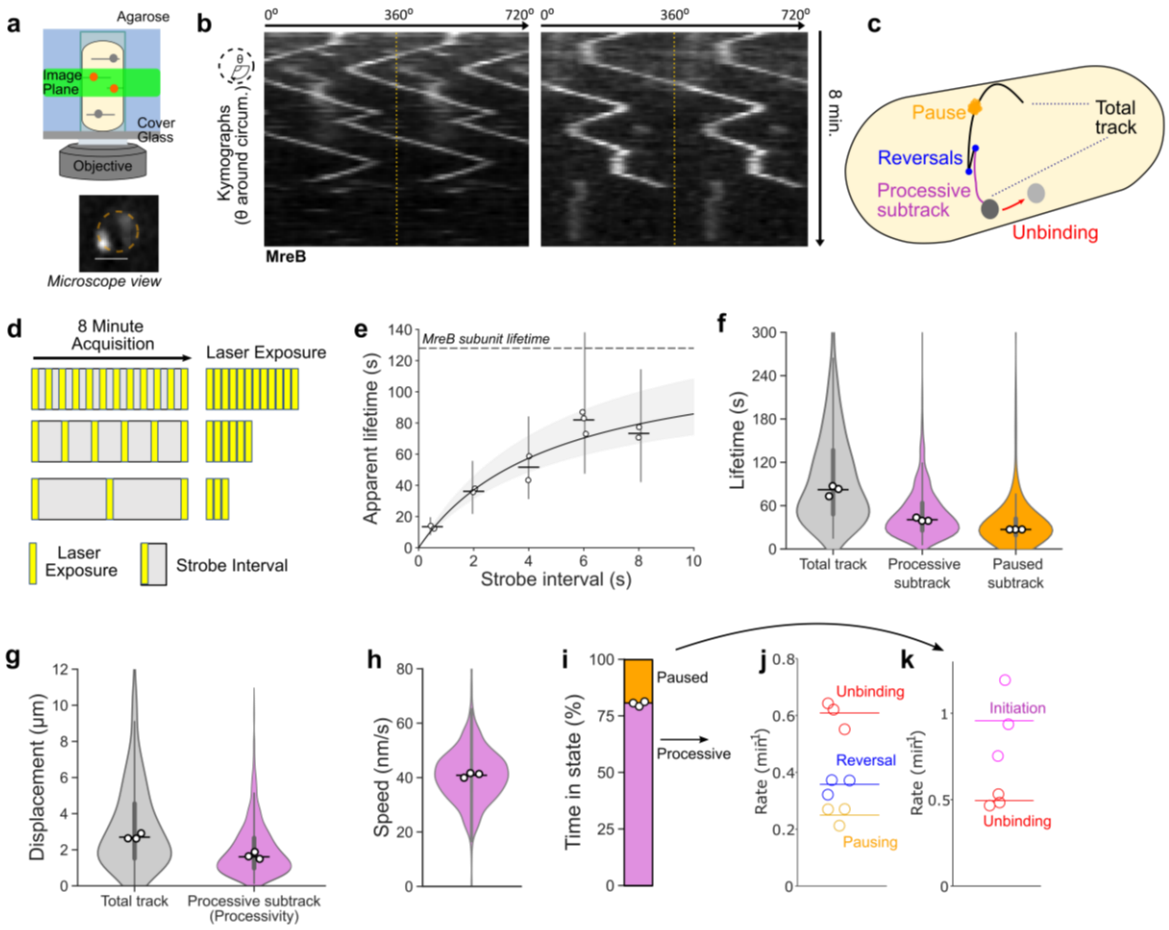

Figure 1: Single molecule VerCINI (smVerCINI) measurements of MreB dynamics. (a) Principle of smVerCINI. Grey lines represent individual MreB filaments, orange circles indicate MreB subunits sparsely labelled with JF549 fluorophore. **(b)** Exemplar kymographs of MreB filament dynamics. Kymographs are measured around the cell circumference. Two full revolutions around the cell (0–720°) are plotted side-by-side to resolve filament trajectories that pass 0°/360°, separated by yellow dotted lines. **(c)** Cartoon illustrating different types of MreB filament dynamics observed. **(d)** Principle of stroboscopic illumination: increasing intervals between constant illumination time reduce photobleaching and allow estimation of photobleaching rate and molecule unbinding rate. **(e)** Stroboscopic illumination plot of strobe interval versus apparent MreB subunit lifetime. Black line: non-linear fit of Gebhardt model (Methods). Grey area: 95% CI on fitted model. Horizontal dashed line: estimated MreB subunit lifetime. Vertical lines: IQR of apparent lifetimes. Fitted subunit lifetime τ_{off}=128 s [95% CI: 109, 164], photobleaching lifetime, τ_{bl}=13s [95% CI: 11, 16]. **(f-g)** MreB filament lifetime and circumferential track displacement for individual tracks and processive or static subtracks. Total tracks refer to the whole observed elongasome trajectory, whereas subtracks refer to regions within a track whose motion type remains constant,

144 i.e. constant processive motion or pausing. **(h)** MreB filament speed for processive subtracks. **(i)** Time MreB
145 filaments spend in each motion state. **(j-k)** Single molecule switching rates for MreB processive subtracks **(j)** and
146 static subtracks **(k)**. Measurements in *b,* f-k performed at 6 s strobe interval. White filled circles: median of
147 biological replicates. Horizontal lines: median of all data points. Violin plots: thick error bar lines indicate IQR,
148 thin lines indicate adjacent vales. Strain used: *B. subtilis* SM01 (*mreB-HaloTag, Δhag*).

149 We next characterized MreB motility by smVerCINI. We chose a strobe interval of 6 s, which extended
150 the effective photobleaching lifetime 12-fold to 156 s [95% CI: 132, 192] (Fig. 1e), longer than the
151 median observed MreB subunit lifetime of 128s [95% CI: 109, 164]. This allowed direct measurements
152 of MreB single molecule switching kinetics. We found that MreB filaments are motile 81 % of the time,
153 [Range: 79-81, *n=3*], and immobile (paused) the rest of the time (Fig. 1i). MreB filaments frequently
154 switch between motile and paused states, and motile MreB filaments frequently switch direction
155 (reversal), which likely corresponds to initiation of PG synthesis in the opposite direction (Fig. 1i-k), SI
156 Fig 10d). The median lifetimes of both the processive and paused motility states were substantial: 40.5
157 s [95% CI: 39.0, 43.0] and 27.0 s [95% CI: 24.0, 29.5], respectively (Fig. 1f).

158 While elongasome pauses and reversals have been observed before, they were previously thought to
159 be rare events [11,14], likely due to elongasome trajectory truncation due to TIRF imaging. Strikingly
160 however, we found that 51 % [Range: 48-52, *n=3*] of elongasome processive synthesis events are
161 terminated by changes in elongasome dynamics - reversal or pausing – rather than by elongasome
162 disassembly or MreB dissociation (Fig. 1j). These data thus demonstrate that bidirectional elongasome
163 motility is a central feature of elongasome dynamics. Furthermore, given that so many synthesis
164 events terminate due to changes in motility state rather than disassembly/ dissociation, elongasome
165 bidirectional motility must play a significant role in determining elongasome processivity. The
166 positions of elongasome reversals and pauses did not show any obvious pattern, suggesting that such
167 switching dynamics are caused by intrinsic factors within the elongasome, rather than local
168 heterogeneity in the cell wall template.

169 Using smVerCINI, we found that MreB filaments, and therefore *B. subtilis* elongasomes, are highly
170 processive. Complete MreB tracks were found to contain multiple substates, where MreB was
171 observed either to move processively in the same direction at constant speed – corresponding to
172 active cell wall synthesis [8–10], or to pause for extended periods. Processive subtracks were found
173 to have a median displacement of 1.61 µm [95% CI: 1.51, 1.69] (Fig. 1g), or approximately 180° around
174 the cell circumference (Supplmentary Figure 3). This is substantially greater than the 0.5 µm previously
175 estimated by TIRF [11]. We found that MreB moved at constant speed of 41 nm/s [95% CI: 40, 41],
176 independent of the processive subtrack lifetime (Fig. 1h, SI Fig. 2b). The speeds we observed were
177 similar to those measured previously [8,9]. As this processivity likely determines the initial length of
178 elongasome-synthesized glycan strands, these data support a model where the elongasome-
179 synthesized peptidoglycan strands act as major reinforcing structural elements in the cell sidewall,
180 much like hoops around a barrel.

181 Given that cell wall synthesis rates correlate with cell growth, we wondered how cell growth rate
182 affected elongasome processivity. Surprisingly, we found that large 3-fold changes in growth rate have
183 only a modest effect on elongasome processivity and switching dynamics (SI Fig. 6). Deletion of *mltG*,
184 which has been proposed as a possible terminator of peptidoglycan synthesis [15] also showed
185 minimal effect on elongasome processivity (SI Fig. 7).

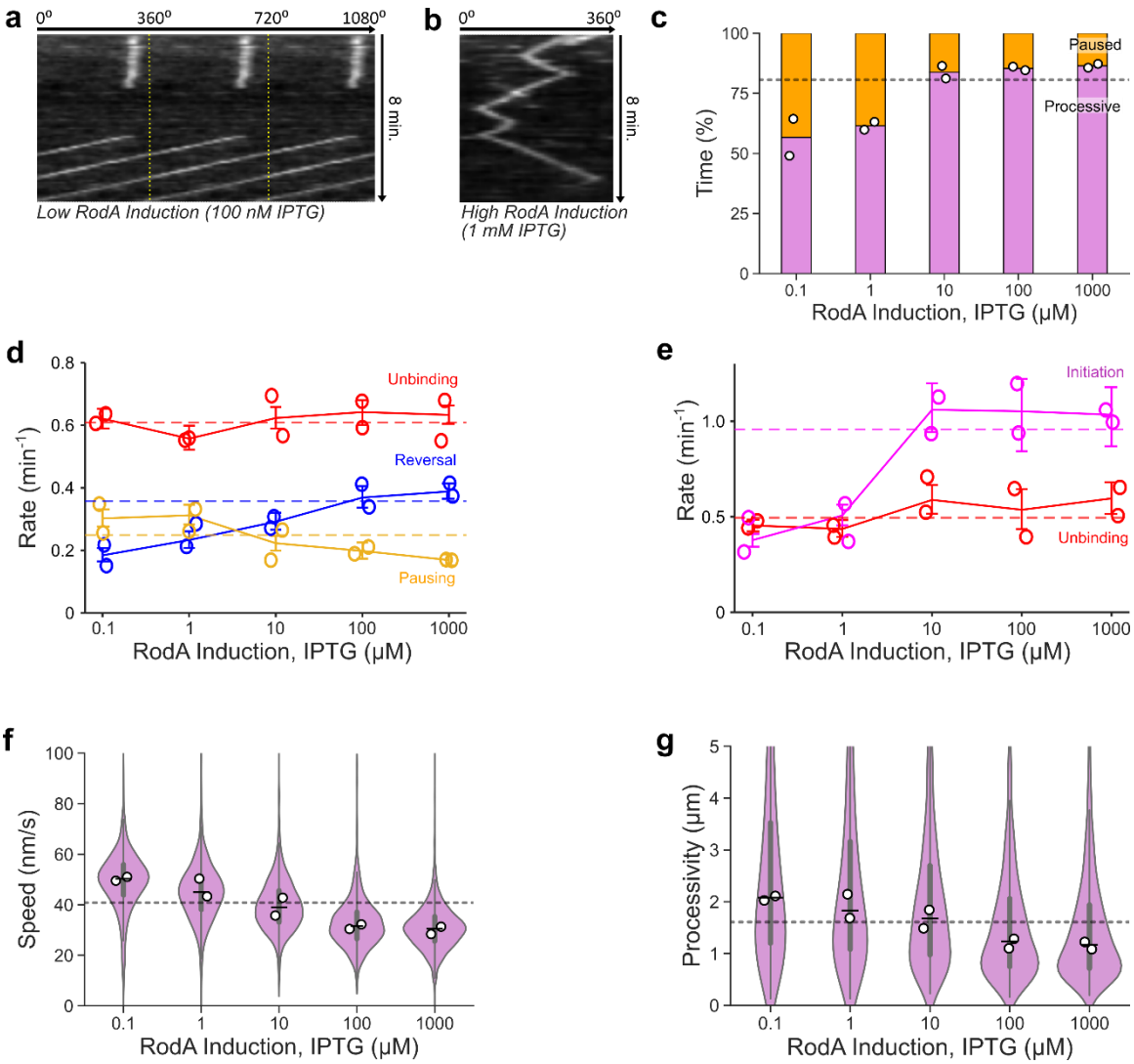

Figure 2: Effect of cellular levels of RodA on MreB dynamics. (a-b) Exemplar kymographs of MreB filament dynamics at low **(a)** and high **(b)** RodA levels achieved through expression from an IPTG-inducible promoter. Kymographs are measured around the cell circumference. More examples are shown in Supplementary Figure 9. **(c)** Time MreB filaments spend in each motion state as a function of *rodA* expression level. **(d-e)** Single molecule switching rates for MreB processive subtracks **(d)** and static subtracks **(e)**. Solid coloured lines represent medians of all data points for each condition. **(f-g)** MreB filament speed and processivity for processive subtracks. White filled circles: median of biological replicates. Horizontal dashed lines: value of each parameter (eg rate, speed) at native *rodA* expression level in strain SM01 (*mreB-HaloTag, Δhag*). Narrow horizontal lines: median of all data points. Violin plots: thick error bar lines indicate IQR, thin lines indicate adjacent values. Strain used: *B. subtilis* SM28 (*mreB-HaloTag*, *Pspac-rodA, Δhag*). Further quantification in Supplementary Figure 7.

RodA expression level regulates bidirectional motility and elongasome processivity

It was previously speculated that elongasome reversals could be caused by molecular motor tug-of-war, whereby two or more RodA-PBP2A/ PBPH synthesis complexes attached to a symmetrical MreB-filament pull in opposite directions [18], similar to eukaryotic organelle transport [16]. However, this proposal was not widely accepted as bidirectional motility of elongasomes was until now assumed to be a rare, inconsequential feature of elongasome dynamics, as well as due to other limitations in the original tug-of-war model, outlined in the next section.

Given our frequent observation of elongasome reversals and pauses, which are strongly reminiscent of eukaryotic molecular motor tug-of-war, we decided to revisit the elongasome tug-of-war model. In

206 the eukaryotic model, cargo such as lipid droplets is transported bidirectionally along microtubules by
207 competing molecular motors which constantly attempt to drag the cargo in opposite directions [17].
208 In the elongasome tug-of-war model, the molecular motors (peptidoglycan synthases) move
209 processively along the cell wall track, which is analogous to the microtubule track in the eukaryotic
210 model. The cargo in the case of the elongasome is the MreB filament. PG synthesis results in
211 processive motion of both the elongasome synthases and the MreB filament relative to the cell wall
212 (Fig. 3a, SI Fig. 10). Motor competition in the case of the elongasome corresponds to attempts by
213 synthesis complexes to initiate cell wall synthesis in the opposite direction to the current direction of
214 elongasome cell wall synthesis (Fig. 3a, SI Fig. 10).

215 We set out to test whether elongasome complexes might indeed participate in molecular motor tug-
216 of-war, and to determine whether tug-of-war mediated reversals might thereby determine
217 elongasome processivity. We titrated cellular levels of the elongasome transglycosylase RodA in a
218 strain with inducible expression from the native locus (*rodA':P$_{spac}$-rodA* [2]), and measured
219 elongasome dynamics by smVerCINI of MreB-HaloTag. At low *rodA* expression levels, we observed
220 that elongasomes exhibited extended pauses, infrequent reversals, and high speed (Fig. 2,
221 Supplementary Videos 4-8). In contrast, at high *rodA* expression levels, pauses were rare, reversals
222 more frequent and speeds lower (Fig. 2d, Supplementary Videos 9-13). MreB pausing rate decreased
223 0.43-fold (-0.13 min^{-1} difference [95% CI: -0.17,-0.10]), reversal rate increased 1.1-fold (0.20 min^{-1}
224 difference [95% CI: 0.17,0.24]) and motile MreB speed decreased 0.39-fold (-20 nm s^{-1} difference [95%
225 CI:-20 ,-19]) at high vs low *rodA* expression levels (1mM IPTG vs 100 nM IPTG induction, Figure 2d,f).
226 No change was detected in MreB unbinding rate (0.01 min^{-1} difference [95% CI: -0.03,0.06] (Fig. 2d),
227 consistent with MreB movement being driven by peptidoglycan synthesis rather than MreB
228 polymerisation/depolymerisation. Intriguingly, MreB processivity decreased 0.44-fold, (-0.91 µm
229 difference [95% CI: -1.0, -0.78]) between high and low *rodA* expression, and the processivity of cells
230 expressing *rodA* from the native promotor was near the mid-point of this range (Fig. 2g).

231 Together, these data show that elongasome dynamics and processivity are sensitively regulated by
232 the cellular concentration of RodA. The data are consistent with a model where increased RodA levels
233 lead to more active synthesis complexes bound to each MreB filament, thereby causing more frequent
234 incidences of tug-of-war between oppositely oriented synthesis complexes, leading to frequent and
235 rapid elongasome reversals. These data are also consistent with a model where high levels of tug-of-
236 war reduce the overall elongasome processivity by more frequent reversals and reduced average
237 elongasome speed due to drag from competing synthesis complexes.

238 One possible alternative model is that elongasome reversals could be caused by collisions between
239 two elongasome complexes. TIRF-structured illumination microscopy (SIM) has previously been used
240 to observe isolated MreB filaments undergoing reversals without any other filaments nearby to collide
241 with, inconsistent with the collision model [8,18]. In a third model, elongasome reversals could be
242 caused by interactions with existing peptidoglycan; if, for example, glycans oriented at certain angles
243 could act as effective barriers to the elongasome. While it is possible that interactions with the
244 peptidoglycan may play some role in elongasome bidirectional motility, that model does not explain
245 why elongasome reversal rate increases, or why pausing rate decreases, as *rodA* expression level is
246 increased.

247 We also tested how single knockouts of the redundant elongasome transpeptidases PBP2A (*pbpA*) and
248 PBPH (*pbpH*) affected elongasome dynamics. Deletions of these genes had little effect on elongasome
249 switching kinetics, speed or processivity (SI Fig. 4, Supplementary Table 6). This is consistent with
250 previous observations whereby overexpression of individual elongasome transpeptidases alone did
251 not affect cell width [2]. In addition, the elongasome transpeptidase in *E. coli* is produced to levels
252 where most of the protein is freely diffusive and not bound to the elongasome [19]. Together, these

253 results support a model where the elongasome transpeptidases are in excess compared to RodA, and
254 thus not the limiting factor in elongasome activity. Our data show that RodA concentration, or its
255 assembly to an elongasome complex, is a principal factor controlling the concentration of active
256 elongasome synthesis complexes within the cell any given time.

257 We also considered whether cellular levels of lipid II could play a role in regulating elongasome
258 dynamics. Overexpressing *murAA*, an enzyme at the beginning of the lipid II synthesis pathway has
259 previously been observed to lead to increased lipid II cellular levels and altered cell growth rate in
260 minimal medium [20]. However, upon overexpression of *murAA* in minimal medium we did not
261 observe changes in cell growth rate and morphology, elongasome processivity or elongasome speed
262 relative to native *murAA* expression levels (Supplementary Figure 8, Supplementary Table 6),
263 suggesting that lipid II levels do not rate limit cell growth under our experimental conditions.
264 Additionally, if lipid II levels dropped substantially upon *rodA* overexpression because of the presence
265 of more enzymes to consume the substrate, the likely consequences for elongasome dynamics would
266 be that elongasome complexes (i) pause or terminate synthesis more frequently and/ or (ii) unbind or
267 disassemble more frequently. We observe neither of these effects in our data (Figure 2D). At last,
268 substrate limitation cannot plausibly explain the observed increased rate of elongasome reversals
269 upon *rodA* overexpression, as this requires the same or higher levels of elongasome activity, not less.
270 These data indicate that cellular lipid II levels are unlikely to play a major role in regulating elongasome
271 bidirectional motility.

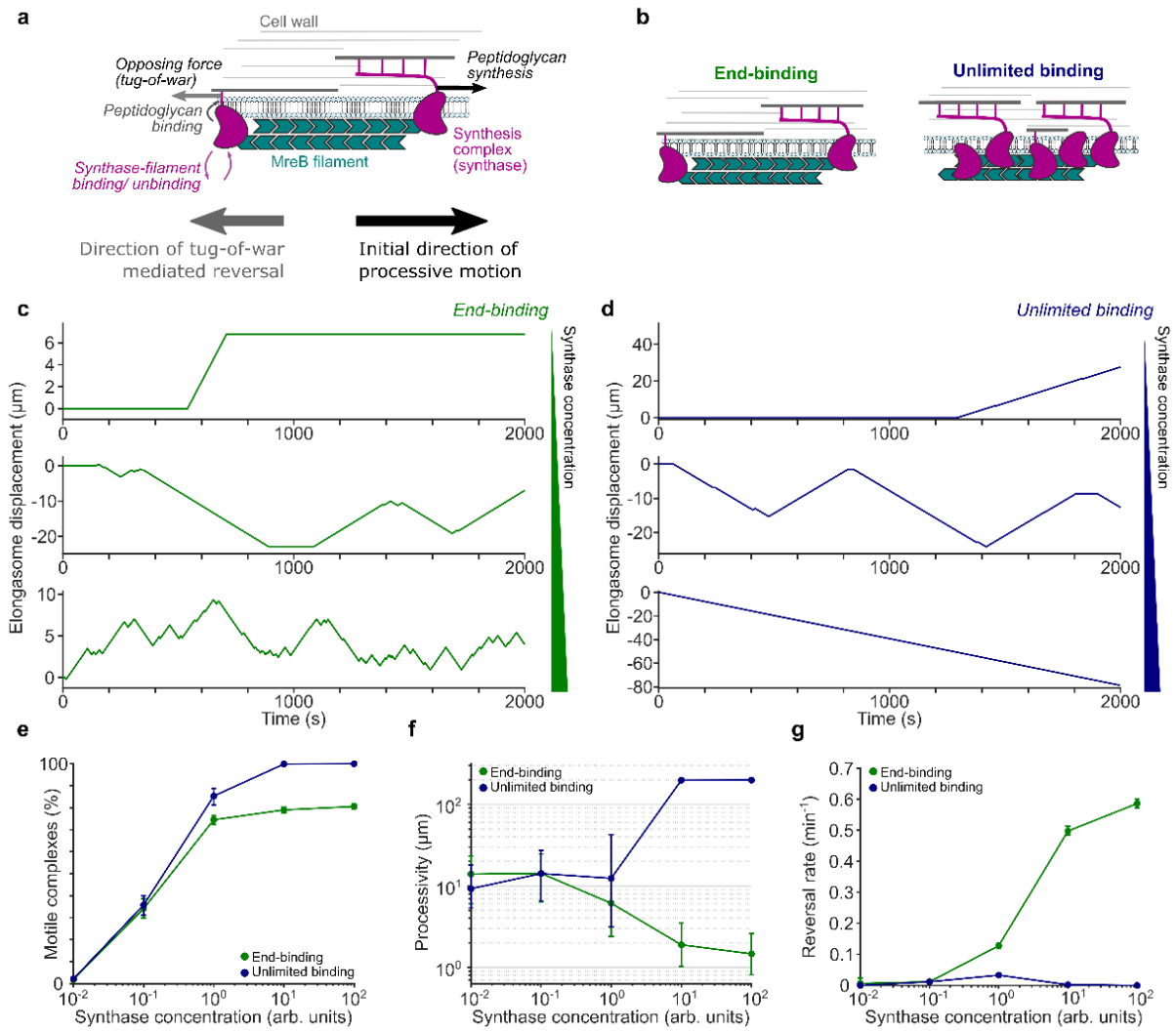

Figure 3: Simulations of elongasome tug-of-war dynamics. (a) Cartoon of elongasome complex dynamics as implemented in the stochastic model. **(b)** Illustration of the two models of elongasome tug-of-war tested: *end-binding*, where only one synthesis complex can bind to each end of the antiparallel MreB double filament, in opposite directions; *unlimited binding*, where multiple synthesis complexes can bind along the MreB filament. **(c-d)** Examples of simulated elongasome dynamics at low (10^{-2} arb. Units), intermediate (10^{0} arb. Units) and high (10^{2} arb. Units) synthesis complex (synthase) concentrations for end-binding and unlimited binding models. **(e-g)** Fraction of motile elongasomes, their processivity and reversal rate as a function of synthesis complex concentration for both models. Solid coloured lines with filled circles, sample medians; vertical lines, 95% CI.

Stochastic simulations show that an end-binding tug-of-war model can explain experimentally observed effects of RodA expression level on elongasome processivity and bidirectional motility

Previously, it was proposed that elongasome tug-of-war between many synthases bound along the entire MreB filament might regulate elongasome dynamics [18]; a scenario which we term the *unlimited binding* elongasome tug-of-war model (Fig. 3b). However, this model was not widely accepted as the bidirectional motility of elongasomes was until now assumed to be a relatively unimportant feature of elongasome dynamics, mostly due to underestimation of elongasome pausing and reversal rates [11,14]. The *unlimited-binding* tug-of-war model also assumed a large numbers of competing synthesis complexes bound to a single MreB filament, which has since been found to be unlikely [5] and predicted a strong dependence of elongasome speed upon MreB filament length

292 which was later found not to be the case [5]. Furthermore, previous theoretical work on eukaryotic
293 molecular motors showed that as more molecular motors are added to an *unlimited-binding* tug-of-
294 war scenario, a runaway scenario occurs where reversals become exponentially less likely as a single
295 opposing motor must win the tug-of-war against an ever-greater number of engaged motors [17].
296 Taken together, the *unlimited-binding* model is not easy to reconcile with our observations that MreB
297 reversal rate increases and processivity decreases at high RodA levels. To address this, and inspired by
298 the observation that MreB forms a symmetric antiparallel double filament [4], we propose an *end-*
299 *binding* elongasome tug-of-war model, where at most two synthesis complexes can bind to an MreB
300 filament, one at each end, pointing in opposite directions (Fig. 3b). The *end-binding* model inherently
301 avoids large numbers of synthesis complexes per filament, as well as the highly processive multi-motor
302 scenario. Alternatively, we speculated that the *unlimited-binding* model might potentially be able to
303 explain our experimental observations if cellular concentrations of elongasome synthesis complex
304 components are low enough to limit the number of synthesis complexes per MreB filament to around
305 1-2 on average, and thereby mostly avoid the runaway elongasome scenario.

306 To test these two models, we used Monte Carlo simulations to evaluate whether either the *end-*
307 *binding* or *unlimited-binding* synthase tug-of-war models are physically plausible mechanisms to
308 regulate elongasome reversal rate and processivity. The simulations are an extension of the Müller,
309 Klumpp, and Lipowsky (MKL) model of eukaryotic cargo transport [17], and assume that multiple
310 RodA-bPBP synthesis complexes can bind to both the MreB filament and the existing cell wall to
311 initiate peptidoglycan synthesis (Fig. 3a, Supplementary Note 1). Synthesis complexes attempting to
312 perform peptidoglycan synthesis in opposite directions will stall and briefly engage in tug-of-war,
313 resulting in either resumption of peptidoglycan synthesis in the original direction, or reversal and
314 initiation of peptidoglycan synthesis in the opposite direction.

315 We performed simulations of each model over a range of synthesis complex concentrations, using an
316 extension of the MKL model to allow concentration dependent binding/ unbinding of synthesis
317 complexes from the MreB filament (Fig. 3, SI Fig. 10, SI Note 1). Both models showed extended
318 elongasome pausing and infrequent reversals at low synthesis complex concentrations (Fig. 3), similar
319 to our experimental measurements (Fig. 2). At intermediate synthesis complex concentration,
320 elongasome reversal rate increased for both the *end binding* and *unlimited binding* models. At high
321 synthesis complex concentrations, the *end binding* model still showed frequent reversals, consistent
322 with our experimental data. However, the reversal rate for the *unlimited binding model* declined
323 rapidly once the average number of bound synthesis complexes increased beyond two (Fig. 3g).

324 We also found that as synthesis complex concentration increased, the *end binding* model processivity
325 decreased in a manner consistent with our experimental observations. While the *unlimited binding*
326 model shows a transient increase in reversal rate at intermediate synthase concentrations, which
327 could potentially partially reproduce experimental results, even in this regime we were not able to
328 reproduce the experimentally observed increase in processivity as a function of synthase
329 concentration in simulations of the *unlimited binding* model as implemented here. Consistent with
330 previous analyses of the MKL model for eukaryotic motor tug-of-war [17], at high synthase
331 concentration the *unlimited binding* model predicts almost indefinitely processive elongasomes -
332 limited here only by the length of the simulations. This is because individual elongasomes are very
333 unlikely to win a tug-of-war against large numbers of oppositely bound active synthases. This runaway-
334 motor scenario is inconsistent with experimental results.

335 These data show that an *end-binding* synthase tug-of-war model is a physically plausible model that
336 is sufficient to recapitulate experimentally observed trends in elongasome reversal rate and
337 processivity. Interestingly, this model also makes strong predictions about the structure, location and

338 number of RodA-bPBP complexes on MreB filaments, which could be tested in future to better
339 understand the molecular mechanisms underlying elongasome tug-of-war.

340 **Cell widening upon *rodA* overexpression may be driven by tug-of-war mediated reduction in**
341 **elongasome processivity**

342 RodA protein levels have previously been shown to control *B. subtilis* cell width in a non-trivial
343 manner [2]: low or high RodA levels lead to abnormally wide cells, whereas intermediate levels ensure
344 narrower, wild-type-like cell morphology. We confirmed that the cell widening phenotype upon *rodA*
345 overexpression also occurred in the minimal media and culture conditions used in this study (Fig. 4a,
346 SI Fig. 12).

347 Recent studies support a model where that cellular levels of motile elongasomes determine cell width
348 by controlling the density of newly synthesized circumferentially oriented glycan strands and thus
349 regulating lateral cell wall stiffness. This model predicts that cell width decreases as elongasome
350 synthase concentration increases [2]. However, this model is insufficient to explain the increase in cell
351 width upon overexpression of *rodA* [2]. We found that cell widening upon *rodA* overexpression (1 mM
352 IPTG) is not associated with any detectable change in surface density of motile MreB filaments
353 compared to induction with 10 µM IPTG (0.36 track density μm^{-2} difference [95% CI: -0.54, 1.3]) (Fig.
354 4b, SI Table 6), which have previously been shown to regulate cell width [2], nor any detectable change
355 in cell growth rate (SI Fig. 12).

356 Our findings that RodA levels determine elongasome processivity via tug-of-war mediated regulation
357 (Fig. 2-3) provide a simple mechanistic model for the complex dependence of cell width on cellular
358 RodA levels. We hypothesize that cells must maintain a balance between: (i) elongasome pausing at
359 low synthase levels, which reduces cellular levels of motile elongasomes; and (ii) tug-of-war at high
360 synthase levels, which reduces elongasome processivity (Fig. 2). Since elongasome synthesized glycan
361 strands act to reinforce the cell sidewall, both the length and total number of elongasome synthesized
362 glycans should determine cell sidewall stiffness and width. Therefore, an optimally stiff, narrow cell
363 wall would be synthesized at intermediate synthase concentration levels, which balances the opposing
364 constraints of density of active elongasomes and elongasome processivity (Fig. 5).

365 It was previously speculated that cell widening upon *rodA* overexpression could be caused by high
366 levels of disorganized synthesis by RodA-bPBP complexes not bound to the elongasome [2]. However,
367 experimental evidence has not yet been presented for that hypothesis. Further experiments will be
368 required to conclusively determine whether elongasome tug-of-war, off-target RodA-bPBP synthesis
369 or a combination of both drive cell widening upon *rodA* overexpression.

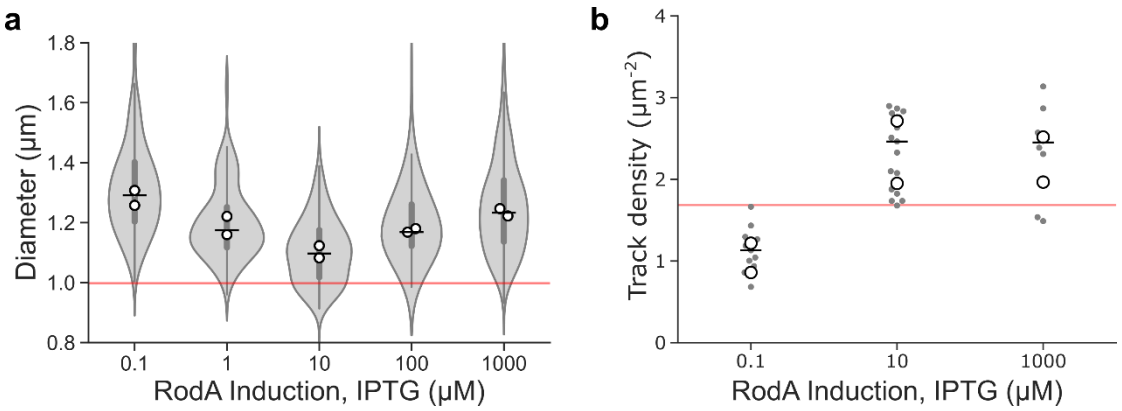

370

371 **Figure 4: Effect of cellular levels of RodA on cell shape and MreB filament density.** Effect of titration of RodA
372 cellular levels expressed as sole cellular copy from an inducible promotor on **(a)** cell diameter, and **(b)** surface
373 density of motile MreB filaments measured by SIM-TIRF microscopy. Horizontal lines show overall median.

374 Vertical lines indicate IQR. White filled circles indicate biological replicates. Grey filled circles indicate medians
375 of each field of view in SIM-TIRF experiments. Red line indicates values for native RodA levels. Strain used: *B.*
376 *subtilis* SM28 (*mreB-HaloTag*, *Pspac-rodA, Δhag*).

377 **DISCUSSION**

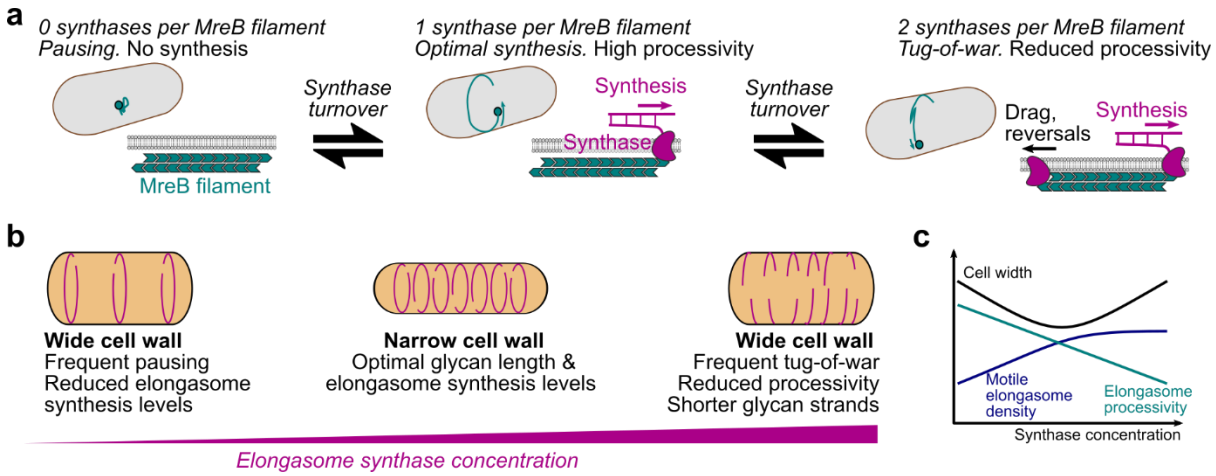

378

379 **Figure 5: Tug-of-war model of elongasome dynamics and cell size regulation. (a)** Model for effect of number of
380 bound active synthesis complexes on elongasome dynamics. Note that synthases refer to complete synthesis
381 complexes, i.e., active RodA-bPBP pairs. **(b-c)** Speculative model for effect of elongasome synthase
382 concentration on cell shape.

383 The elongasome plays a central role in cell wall growth and maintenance of cell shape in a wide range
384 of bacteria. In this study, we found that *B. subtilis* elongasomes are highly processive with each event
385 covering on average half the cell circumference, thus supporting a model in which elongasome
386 synthesized glycan strands function as major structural elements that reinforce the cell sidewall. We
387 found that bidirectional motility – reversal and pausing – is not a rare curiosity as previously thought
388 but rather a central feature of elongasome dynamics. We showed that elongasome processivity and
389 bidirectional motility are regulated by molecular motor tug-of-war between multiple elongasome
390 synthesis complexes. Our data also provide initial evidence for an end-binding tug-of-war between
391 maximally two synthesis complexes bound to opposite ends of the antiparallel MreB filament (Figure
392 5a). We also found evidence that elongasome tug-of-war may regulate cell size and shape via
393 modulation of elongasome processivity, and thereby the length of new glycan strands (Figure 5). These
394 results establish molecular motor tug-of-war acts as a major regulator of bacterial cell wall synthesis
395 activity.

396 Our study shows that molecular motor tug-of-war regulates MreB-cytoskeleton-associated cell wall
397 synthesis in the model bacterium *B. subtilis*. This phenomenon, previously thought to be exclusive to
398 eukaryotes, is the first of its kind described on a molecular level in bacteria. Similar to bidirectional
399 molecular motor transport in eukaryotes [16], molecular motor tug-of-war enables straightforward
400 tuning of synthase dynamics, and could thereby facilitate rapid regulation of cell wall material
401 properties, by regulating the concentration or activity of the Rod-complex. Tug-of-war mediated
402 bidirectional motility may also allow obstacles in the cell wall to be avoided and peptidoglycan
403 synthesis to be distributed evenly around the surface of the cell wall. Further studies will be required
404 to determine the molecular principles underlying elongasome tug-of-war and the role of molecular
405 motor tug-of-war in regulating bacterial cell shape.

ACKNOWLEDGEMENTS

We thank Yoshi Kawai, Jeff Errington, Richard Daniel (Newcastle) and Ethan Garner (Harvard) for strains. We thank Charles Winterhalter (Newcastle) for plasmids. We thank Cees Dekker (TU Delft, Netherlands) for nanofabricated VerCINI wafers and Luke Lavis (Janelia Farm, USA) for Janelia Fluor dyes. SH acknowledges funding support by a Wellcome Trust & Royal Society Sir Henry Dale Fellowship grant number 206670/Z/17/Z and a UK Biotechnology and Biological Sciences Research Council (BBSRC) grant BB/X001482/1. SM was supported BBSRC doctoral studentship (BB/M011186/1). HS acknowledges funding from BBSRC grants BB/S00257X/1 and BB/X001512/1.

AUTHOR CONTRIBUTIONS

SM, MB and JG constructed and characterised bacterial strains. SM, MB, AM, DMR and SH performed experiments. SM, AM, DMR, HS and SH analysed data. ZS and TB developed PureDenoiseGPU software. KW tested PureDenoiseGPU software. SH performed simulations. JE designed and built one of the custom microscopes used in the study. SH, SM and HS designed experiments. SH and HS directed the research. SH and SM wrote the manuscript with input from all authors.

420 **MATERIALS AND METHODS**

421 **Bacterial strains and growth conditions**

422 Strains used in this study are listed below. Strains were streaked from -80°C freezer glycerol stocks
423 onto Nutrient Agar (NA) plates containing the relevant antibiotics and/or inducers and grown
424 overnight at 37°C. Starter cultures were prepared from a single colony in $S750^{glucose}$ media and grown
425 with orbital agitation at 175 rpm overnight at 37°C. The next day, overnight cultures were diluted to
426 an OD_{600} of 0.05-0.1 in $S750^{glucose}$ media and grown at 30°C with orbital agitation at 175 rpm with any
427 required inducer until they reached the appropriate OD_{600}. Liquid cultures were grown in flasks with
428 at least a 1:20 culture to flask volume ratio. Overnight cultures were grown in either 2 ml or 5 ml
429 volumes, where day cultures were always grown in 5 ml volumes.

430 Microscopy was performed at 30°C. When necessary, antibiotics and inducers were used at the
431 following final concentrations: chloramphenicol 5 µg/ml, spectinomycin 60 µg/ml, erythromycin
432 1 µg/ml, lincomycin 10 µg/ml, kanamycin 5 µg/ml. S750 media contains 1 X S750 salts, 1 X Metal mix,
433 10 mM L-Glutamate (Sigma) and 1 % carbon source (Glucose or Maltose (VWR)). Metal mix was
434 prepared as a 100 X stock comprising of 2 mM Hydrochloric Acid (HCl) (Honeywell), 190 mM
435 Magnesium Chloride Hexahydrate (Sigma), 65.9 mM Calcium Chloride Dihydrate (Sigma, 4.84 mM
436 Manganese Chloride Tetrahydrate (Fisher), 0.106 mM Zinc Chloride (Sigma), 0.196 mM Thiamine
437 Chloride (Sigma) and 0.470 mM Iron (III) Chloride Hexahydrate (VWR). S750 salts were prepared as a
438 10 X stock containing 500 mM MOPS (Sigma), 100 mM Ammonium Sulphate (Sigma), Potassium
439 Phosphate Monobasic (VWR) with pH adjusted to 7.0 with Potassium Hydroxide (VWR).

440 We found that the following considerations were important for reproducible results: (1) S750 must be
441 made up fresh from the relevant stock solutions no more than 1-2 days before the experiments (see
442 S750 preparation protocol in Supplementary Note 2). (2) cells must be cultured in highly aerobic
443 conditions, here in 2-5 ml volumes in 125 ml conical flasks – notable *not* in 16 ml volume test tubes,
444 (3) exponential growth phase cells should be given 10 minutes to recover after being immobilized on
445 the agarose pad before acquiring microscopy data. Deviations from these requirements led to
446 decreased elongasome speed or reduced ratio of motile: immobile elongasomes.

447 **Strain construction**

448 All strains are derived from the PY79 strain [21]. All experimental strains were constructed with the
449 *Δhag* mutant to disable flagellar motility and reduce cell chaining for VerCINI experiments [12].
450 *B. subtilis* was transformed in accordance with standard protocols [22]. Oligonucleotides and strains
451 used in this study are detailed in Supplementary Table 2.

452 SM01 (*mreB::mreB-HaloTag, Δhag*) was constructed by transforming bYS40 (Hussain et al. 2018) with
453 gDNA containing *hag::erm* from the *Bacillus* erythromycin (BKE) deletion library (Koo et al. 2017),
454 selecting for transformants on erythromycin and lincomycin. The strain was confirmed by PCR
455 amplification of the *hag* region using oSM01 and oSM02.

456 SM28 (*mreB::mreB-HaloTag, Δhag, rodA':-Pspac-rodA,*) was produced by transforming SM01 with
457 gDNA from YK2245 (Emami et al. 2017). Transformants were selected on 100 µM IPTG and kanamycin.
458 The strain was confirmed by amplification of the *rodA* region using oSM15 and oSM43. In addition,
459 the strain was streaked on NA plates in the presence and absence of 100 µM IPTG and was found to
460 be IPTG dependent.

461 SM22 (*mreB::mreB-HaloTag, Δhag , ΔpbpA*) was constructed by transforming SM01 with gDNA
462 containing *pbpA::kan* from the *Bacillus* kanamycin (BKK) deletion library (Koo et al. 2017), selecting

463 for transformants on kanamycin. The strain was confirmed by PCR amplification of the *pbpA* region
464 using oSM19 and oSM20.

465 SM23 (*mreB::mreB-HaloTag, Δhag, ΔpbpH*) was constructed by transforming SM01 with gDNA
466 containing *pbpH::kan* from the *Bacillus* kanamycin (BKK) deletion library (Koo et al. 2017), selecting
467 for transformants on kanamycin. The strain was confirmed by PCR amplification of the *pbpH* region
468 using oSM27 and oSM28.

469 SM41 (*mreB::mreB-HaloTag, Δhag, ΔmltG*) was constructed by transforming SM01 with gDNA
470 containing *mltG::kan* from the *Bacillus* kanamycin (BKK) deletion library (Koo et al. 2017), selecting for
471 transformants on kanamycin. The strain was confirmed by PCR amplification of the *mltG* region using
472 oSM78 and oSM79.

473 MB60 (*mreB::mreB-HaloTag, Δhag, rod'A:-Pspac-rodA, amyE::tet pveg-we*) and MB59 (SM28,
474 amyE::tet pveg-empty) were constructed by transforming SM28 with the plasmids MB12 and MB13,
475 respectively. Transformants were selected on 100 µM IPTG and tetracycline. Insertion in *amyE* locus
476 was confirmed by iodine assay. In addition, the strains were streaked on NA plates in the presence
477 and absence of 100 µM IPTG and were found to be IPTG dependent.

478 MB36 (*mreB::mreB-HaloTag, Δhag, rodA':-Pspac-rodA, murAA::spec pxyl-murAA*) was constructed by
479 transforming SM28 with gDNA from the strain SLA039 (*murAA:: spec pxyl-murAA*). Transformants
480 were selected on 100 µM IPTG, 0,3% xylose and spectomycin. To confirm insertion in *murAA* locus,
481 the strain was streaked on NA in presence and absence of xylose and was found to be xylose
482 dependant. In addition, the strain was streaked on NA plates in the presence and absence of 100 µM
483 IPTG and was found to be IPTG dependent.

484 MB38 (*PY79, amyE::tet Pveg-msfGFP*) was constructed by transforming PY79 with the plasmid MB10.
485 Transformants were selected on tetracycline. Insertion in *amyE* locus was confirmed by iodine-starch
486 assay.

487 MB76 (*PY79, amyE::spec Pxyl-msfGFP*) was constructed by transforming PY79 with the gDNA from the
488 strain JWG184. Transformants were selected on spectomycin. Insertion in *amyE* locus was confirmed
489 by iodine-starch assay.

490 MB37 (*PY79, ΔmreB::neo*) was constructed by transforming PY79 with the gDNA from the strain KS36
491 (Ωneo3427 Δ*mreB*). Transformants were selected on kanamycin and 20mM $MgSO_4$. Absence of *mreB*
492 was confirmed by the inability of the strain to grown without supplemented $MgSO_4$ (20 mM).

493 MB35 (*PY79, Δmbl::zeo*) was constructed by transforming PY79 with the gDNA from the strain MDS19
494 (*168ca trpC2 mbl::zeo*). Transformants were selected on zeomycin and 20mM $MgCL_2$. Absence of *mbl*
495 gene was confirmed by the inability of the strain to grown without supplemented $MgSO_4$ (20 mM).

496 All used strains are available on request to the authors.

497 **Plasmid construction**

498 pMB10 (*bla amyE::pveg-msfGFP tet*): the plasmid pCW433 (kindly gifted by Charles Winterhalter) was
499 amplified with MB-F-64 and MB-F-65. The *msfGFP* gene was amplified from gDNA from JWG184 strain
500 with MB-F-62 and MB-F-63 primers (underlined region) and inserted by Gibson assembly. The plasmid
501 has been sequenced to confirm the correct insertion.

502 pMB12 (*bla amyE::pveg-murAA tet*): the plasmid pCW433 was amplified with MB-F-64 and MB-F-68.
503 The *murAA* gene was amplified from gDNA from BS168 strain with MB-F-66 and MB-F-67 primers

504 (underlined region) and inserted by Gibson assembly. The plasmid has been sequenced to confirm the
505 correct insertion.

506 pMB13 (*bla amyE::pveg-empty tet*): the plasmid pCW433 was amplified with MB-F-64 and MB-F-65
507 and closed by Gibson assembly. The plasmid has been sequenced to confirm the correct sequence.

508 **Growth curves**

509 OD_{600} was measured every 1 hour from cultures prepared as described above (Bacterial strains and
510 growth conditions).

511 **Cell morphology analysis**

512 Cells were prepared for imaging in $S750^{glucose}$ at 30˚C. Once the cultures had reached OD_{600} 0.6 ± 0.1,
513 Nile Red was added to 200 µl of cells to a working concentration of 1 µg/ml, and incubated at growth
514 temperatures for 10 mins, prepared on agarose microscope slides as described below and cell
515 morphology images recorded using the microscope described below. To measure cell width, a straight-
516 line ROI was drawn over the short axis of the cell in FIJI and an intensity profile plotted. The intensity
517 plots were exported to MATLAB where the centre of each peak and the distance between them were
518 determined by fitting to a tilted circle model [12]. To measure cell length, a straight-line ROI was drawn
519 from the pole to pole, or pole to septum and the length measured in FIJI.

520 **Western blotting**

521 For western blot sample preparation, PY79 and SM01 were grown in S750glu while MB35, MB37 and
522 KS60 were grown in LB supplemented with 20mM $MgSO_4$. Overnight cultures of strains were grown
523 at 37°C. The following morning, cultures were diluted to OD_{600}~0.05 in 5 ml (125 ml flask) and grown
524 at 37°C until OD_{600}~0.4. 1 ml of cell culture was harvested by centrifugation and lysed by incubation
525 for 20 min with 200 µl in BugBuster protein extraction reagent supplemented with 1uL of Benzonase
526 nuclease (Millipore), 0,6 µl of lysozyme (10 mg/ml, Sigma) an EDTA free protease inhibitor cocktail
527 (Roche). Protein contents were quantified by Qubit. Protein extract was heat-denatured for 10 min at
528 80°C in NuPAGE LDS Sample Buffer an an equivalent of 2 µg total protein was separated by SDS-PAGE
529 on a NuPAGE 4-12% Tris-Acetate Midi Gel in MOPS buffer (Invitrogen). Protein was transferred to a
530 0.45 µm PVDF Membrane (Cytiva), and MreB or Spo0J were detected using respective in-house
531 polyclonal antibodies and HRP-conjugated anti-rabbit IgG antibody (Sigma). Samples were developed
532 using Clarity Western ECL Substrate (Bio-Rad) and imaged using an ImageQuant LAS 4000 mini
533 Biomolecular Imager (GE Healthcare).

534 **Microscopy**

535 *VerCINI on custom single molecule microscopes.* Two similar custom single molecule microscopes were
536 used for experiments. Cells were illuminated with a 561 nm laser (Obis). A 100x TIRF objective (Nikon
537 CFI Apochromat TIRF 100XC Oil) was used. A 200 mm tube lens (Thorlabs TTL200) and Prime BSI
538 sCMOS camera (Teledyne Photometrics) were used for imaging, giving effective image pixel size of 65
539 nm/pixel. Imaging was done with a custom-built ring-TIRF module operated in ring-HiLO[23] using a
540 pair of galvanometer mirrors (Thorlabs) spinning at 200 Hz. 8 minute time lapses were obtained with
541 500 ms exposure at a power density of 16.9 W/cm^2 at a strobe interval of 6 s unless otherwise stated.
542 Power density was calculated based on 2.5 mW illumination power measured at the sample, over an
543 illumination area of approximately 14,800 μm^2.

544 *Structured Illumination Microscopy on a Nikon N-SIM.* Cells were illuminated a 561 nm laser (CVI
545 Melles-Griot). A 100x TIRF objective (Nikon CFI Apochromat TIRF 100XC Oil) was used for imaging and
546 an Andor iXon DU897 EMCCD camera was used, with a 2.5x magnifier (Nikon) and standard Nikon

547 tube lens, giving an effective image pixel size of 64 nm/pixel. Cells were illuminated in TIRF-SIM mode,
548 using a 2D-striped pattern. Each SIM image was formed from 9 raw images corresponds to 3 stripe
549 angles and 3 stripe phases. SIM reconstruction was performed using proprietary Nikon software which
550 implements the Gustaffson SIM reconstruction algorithm [24]. Reconstruction was carried out in NIS
551 elements using default settings; Illumination modulation contrast was set to 1.00, high resolution
552 noise suppression was set to 1.00 and out of focus blur suppression was set to 0.05.

553 All microscopy was performed on microscopes equipped with incubators to maintain sample and
554 microscope temperature at 30˚C.

555 **Single Molecule HaloTag labelling with JF-549**

556 At OD_{600} of 0.6 ± 0.1, 500 µl cells were incubated for 15 minutes with JF-549 [13] dissolved in dimethyl
557 sulfoxide (DMSO) to a final concentration of 25 pM at 30˚C with shaking at 175 rpm. Stocks were
558 prepared at concentrations to ensure a working DMSO concentration of <1%. Cells were then washed
559 twice in 500 µl pre-warmed media.

560 **Sample preparation for VerCINI microscopy**

561 Agarose microholes were formed by pouring molten 6% agarose dissolved in media (typically
562 $S750^{glucose}$ unless otherwise stated) onto a silicon micropillar array as described previously [12].
563 Patterned agarose was transferred into a Geneframe (Thermo Scientific) mounted on a glass slide, and
564 excess agarose was cut away to ensure sufficient oxygen.

565 Cultures were concentrated 50-fold and 10 µl was applied to the pad, before centrifugation at 3,220
566 RCF for 4 minutes (Eppendorf 5810 centrifuge with MTP/Flex buckets). Pads were then washed with
567 pre warmed media before application of the cover slip (VWR 22 × 22 mm2 Thickness no. 1.5).

568 **VerCINI data analysis**

569 *Pre-processing*

570 Videos were denoised using the ImageJ plugin PureDenoise [25], which is based on wavelet
571 decomposition. For the largest image dataset- 0.5 s frame interval measurements in Figure 1e – a
572 GPU-accelerated version of PureDenoise was developed and used
573 (http://www.GitHub.com/ZikaiSun/PureGpu). This version also corrects a memory leak bug for large
574 images in the original PureDenoise ImageJ plugin. Performance characterization of PureDenoiseGPU
575 is shown in Supplementary Tables 5-6.

576 Denoised videos were registered using the ImageJ plugin StackReg [26]. Cropped region of interest
577 (ROI) movies containing single in-focus cells were manually selected and exported for analysis using
578 the publically available scripts (https://github.com/HoldenLab/Ring_Analysis_IJ)

579 Images were background subtracted and kymographs extracted using a custom fitting model of diffuse
580 out-of-focus cytoplasmic background plus localized protein signal as previously described [12].

581 *Kymograph analysis of MreB single molecule dynamics.*

582 In ImageJ, a segmented line ROI was manually traced over each track, with segments indicating
583 manually identified processive or paused subtracks. For each kymograph, an ROI set was saved. Using
584 a custom FIJI plugin, 'Export_XY_Coords.ijm', the coordinates of each point in each track were
585 exported to a '.csv' file. The coordinates of each track were analysed using custom python script 'Track
586 data analysis-Full_.ipynb', to determine MreB filament binding dynamics including bound lifetime,
587 processivity. The required Analysis code is available: https://github.com/HoldenLab/Kymograph-spt-
588 analysis

589 **Stroboscopic analysis of photobleaching and MreB binding lifetime**.

590 We analysed MreB subunit unbinding lifetime and JF549 photobleaching lifetime using the
591 stroboscopic illumination method of Gebhardt and coworkers [27]. Using a fixed illumination and
592 exposure time of 500 ms, we systematically increased the total time interval between frames, the
593 strobe interval, and measured the apparent lifetime of labelled MreB molecules for each condition
594 (Fig. 1d-e). We calculated the median lifetime of each dataset, with 95 % CIs calculated by
595 bootstrapping. We then fit the median lifetime data to the equation,

596 $$\tau_{obs} = \Delta t \Big/ \left(\frac{t_{exp}}{\tau_{bl}} + \frac{\Delta t}{\tau_{off}}\right),$$

597 where Δt is the strobe interval (the x-axis), τ_{obs} is the apparent lifetime, t_{exp} is the fixed 500 ms
598 exposure time, τ_{bl} is the JF549 photobleaching lifetime and τ_{off} is the MreB subunit unbinding
599 lifetime. By fitting the data to the median apparent lifetimes, we obtained estimates of median τ_{bl}
600 and τ_{off}, rather than mean, consistent with the rest of the statistics in the manuscript. We obtained
601 95 % CI estimates for τ_{bl} and τ_{off} by bootstrap resampling of the inputs into the stroboscopic fitting
602 equation.

603 **Switching rate analysis**.

604 We calculated single molecule switching rates (reversal, pausing, unbinding, initiation) by counting the
605 number of each transition type from immobile or processive states, and dividing by the total duration
606 of all immobile or processive states observed in the dataset [19]. 95 % confidence intervals on the
607 switching rate were calculated by bootstrap sampling of individual tracks from the dataset.

608 **Pveg/Pxyl intensity measurement**

609 MB38 and MB73 were grown in S750glu or S750gly overnight at 37°C. The following morning, cultures
610 were diluted to OD600~0.05 in 5mL (125mL flask), in S750glu or S750gly with 30mM xylose, and grown
611 at 37°C until OD600~0.5. Once the cultures had reached OD600 0.5 ± 0.1, cells were prepared on
612 agarose microscope slides as described below. James Grimshaw FIJI macro has been used to measure
613 cell average fluorescence (GitHub - NCL-ImageAnalysis/General_Fiji_Macros: Assortment of macros
614 for use with Fiji).

615 **Simulations of elongasome dynamics**

616 We implemented stochastic simulations of elongasome tug-of-war using an adaptation of the Müller,
617 Klumpp, and Lipowsky (MKL) model of tug-of-war in eukaryotic cargo transport [4]. The theoretical
618 model and computational parameters are discussed in detail in *Supplementary Note 1*. A schematic
619 diagram of the elongasome tug-of-war model is presented in Supplementary Figure 6.

620 **Statistics**

621 Experiments were conducted in biological duplicate because variation between clonal bacterial
622 samples was low, as estimated based on small range measured in replicate medians, unless otherwise
623 indicated.

624 Averages reported were median values unless otherwise indicated. Medians of biological replicates
625 are shown on figures as white-filled circles. 95% confidence interval of the median, or of the difference
626 of medians, was estimated by bootstrapping. Interquartile range was indicated by IQR. Thick error bar
627 lines in violin plots indicate interquartile range, thin lines indicate adjacent vales. Because variability
628 between single molecules was far greater than the sample-to-sample variation, estimates of
629 uncertainty (95% Cis, IQRs, etc.) were based on the single molecule datapoints. Sample size, indicating

number of tracks/ track segments, technical and biological replicates, as appropriate, is presented for each dataset in Supplementary Table 1.

Effect size estimates and confidence intervals [28] were calculated based on difference of medians using DABEST (Data Analysis with Bootstrap Coupled Estimation [29]) unless stated otherwise, difference of medians using custom bootstrapping scripts (for the switching rate kinetics data), or difference of means and margin of error calculations [28] (for small sample size calculations, ie growth rate and cell diameter). All effect sizes are listed in Supplementary Table 7. In comparison to null hypothesis significance testing (NHST) analysis, which only reports on whether a difference may exist between two populations, effect size analysis addresses one of the flaws of NHST by allowing analysis of not only whether a difference may exist but also the magnitude of that difference [28], which is often of critical importance for interpreting the biological significance of a result. For comparison to NHST analysis, a median/ mean observed difference whose 95% CIs are both greater or less than zero this would indicate rejection of the null hypothesis that the two population medians/ means are equal at $p = 0.05$ significance level.

For estimates of the percentage of the population in a specific state (eg percentage of motile tracks), uncertainty is reported to the full data range (*Range)* of all biological replicates.

DATA AVAILABILITY

Raw data are available on request to the authors and will be uploaded to a public repository prior to journal publication. Bacterial strains are available on request to the authors.

CODE AVAILABILITY

Open source software for image analysis of VerCINI data was previously described and is available on the Holden Lab GitHub page: https://github.com/HoldenLab/VerciniAnalysisJ, https://github.com/HoldenLab/ring-fitting2,
Open source software for kymograph analysis available on the Holden Lab GitHub page: https://github.com/HoldenLab/Kymograph-spt-analysis.git
Open source PureDenoise-GPU denoising software is available on GitHub: http://www.GitHub.com/ZikaiSun/PureGpu.
Open source software for the tug-of-war simulations: https://github.com/HoldenLab/lipowskiModel

REFERENCES

[1] A. Vigouroux, B. Cordier, A. Aristov, L. Alvarez, G. Özbaykal, T. Chaze, E.R. Oldewurtel, M. Matondo, F. Cava, D. Bikard, S. van Teeffelen, Class-A penicillin binding proteins do not contribute to cell shape but repair cell-wall defects, eLife 9 (2020) e51998. https://doi.org/10.7554/eLife.51998.

[2] M.F. Dion, M. Kapoor, Y. Sun, S. Wilson, J. Ryan, A. Vigouroux, S. van Teeffelen, R. Oldenbourg, E.C. Garner, Bacillus subtilis cell diameter is determined by the opposing actions of two distinct cell wall synthetic systems, Nat. Microbiol. 4 (2019) 1294–1305. https://doi.org/10.1038/s41564-019-0439-0.

[3] H. Cho, C.N. Wivagg, M. Kapoor, Z. Barry, P.D.A. Rohs, H. Suh, J.A. Marto, E.C. Garner, T.G. Bernhardt, Bacterial cell wall biogenesis is mediated by SEDS and PBP polymerase families functioning semi-autonomously, Nat. Microbiol. 1 (2016) 16172. https://doi.org/10.1038/nmicrobiol.2016.172.

[4] F. van den Ent, T. Izoré, T.A. Bharat, C.M. Johnson, J. Löwe, Bacterial actin MreB forms antiparallel double filaments, eLife 3 (2014). https://doi.org/10.7554/eLife.02634.

[5] C. Billaudeau, Z. Yao, C. Cornilleau, R. Carballido-López, A. Chastanet, MreB Forms Subdiffraction Nanofilaments during Active Growth in Bacillus subtilis, mBio 10 (2019). https://doi.org/10.1128/mBio.01879-18.

[6] S. Hussain, C.N. Wivagg, P. Szwedziak, F. Wong, K. Schaefer, T. Izoré, L.D. Renner, M.J. Holmes, Y. Sun, A.W. Bisson-Filho, S. Walker, A. Amir, J. Löwe, E.C. Garner, MreB filaments align along greatest principal membrane curvature to orient cell wall synthesis, eLife 7 (2018) e32471. https://doi.org/10.7554/eLife.32471.

[7] S. Dersch, C. Reimold, J. Stoll, H. Breddermann, T. Heimerl, H.J. Defeu Soufo, P.L. Graumann, Polymerization of Bacillus subtilis MreB on a lipid membrane reveals lateral co-polymerization of MreB paralogs and strong effects of cations on filament formation, BMC Mol. Cell Biol. 21 (2020) 76. https://doi.org/10.1186/s12860-020-00319-5.

[8] J. Domínguez-Escobar, A. Chastanet, A.H. Crevenna, V. Fromion, R. Wedlich-Söldner, R. Carballido-López, Processive Movement of MreB-Associated Cell Wall Biosynthetic Complexes in Bacteria, Science 333 (2011) 225–228. https://doi.org/10.1126/science.1203466.

[9] E.C. Garner, R. Bernard, W. Wang, X. Zhuang, D.Z. Rudner, T. Mitchison, Coupled, Circumferential Motions of the Cell Wall Synthesis Machinery and MreB Filaments in B. subtilis, Science 333 (2011) 222–225. https://doi.org/10.1126/science.1203285.

[10] S. van Teeffelen, S. Wang, L. Furchtgott, K.C. Huang, N.S. Wingreen, J.W. Shaevitz, Z. Gitai, The bacterial actin MreB rotates, and rotation depends on cell-wall assembly, Proc. Natl. Acad. Sci. 108 (2011) 15822–15827. https://doi.org/10.1073/pnas.1108999108.

[11] S. Dersch, J. Mehl, L. Stuckenschneider, B. Mayer, J. Roth, A. Rohrbach, P.L. Graumann, Super-Resolution Microscopy and Single-Molecule Tracking Reveal Distinct Adaptive Dynamics of MreB and of Cell Wall-Synthesis Enzymes, Front. Microbiol. 11 (2020) 1946. https://doi.org/10.3389/fmicb.2020.01946.

[12] K.D. Whitley, S. Middlemiss, C. Jukes, C. Dekker, S. Holden, High-resolution imaging of bacterial spatial organization with vertical cell imaging by nanostructured immobilization (VerCINI), Nat. Protoc. 17 (2022) 847–869. https://doi.org/10.1038/s41596-021-00668-1.

[13] J.B. Grimm, B.P. English, J. Chen, J.P. Slaughter, Z. Zhang, A. Revyakin, R. Patel, J.J. Macklin, D. Normanno, R.H. Singer, T. Lionnet, L.D. Lavis, A general method to improve fluorophores for live-cell and single-molecule microscopy, Nat. Methods 12 (2015) 244–250. https://doi.org/10.1038/nmeth.3256.

[14] C. Billaudeau, A. Chastanet, Z. Yao, C. Cornilleau, N. Mirouze, V. Fromion, R. Carballido-López, Contrasting mechanisms of growth in two model rod-shaped bacteria, Nat. Commun. 8 (2017) 15370. https://doi.org/10.1038/ncomms15370.

[15] R. Yunck, H. Cho, T.G. Bernhardt, Identification of MltG as a potential terminase for peptidoglycan polymerization in bacteria, Mol. Microbiol. 99 (2016) 700–718. https://doi.org/10.1111/mmi.13258.
[16] M.A. Welte, Bidirectional Transport along Microtubules, Curr. Biol. 14 (2004) R525–R537. https://doi.org/10.1016/j.cub.2004.06.045.
[17] M.J.I. Müller, S. Klumpp, R. Lipowsky, Tug-of-war as a cooperative mechanism for bidirectional cargo transport by molecular motors, Proc. Natl. Acad. Sci. 105 (2008) 4609–4614. https://doi.org/10.1073/pnas.0706825105.
[18] P. v. Olshausen, H.J. Defeu Soufo, K. Wicker, R. Heintzmann, P.L. Graumann, A. Rohrbach, Superresolution Imaging of Dynamic MreB Filaments in B. subtilis—A Multiple-Motor-Driven Transport?, Biophys. J. 105 (2013) 1171–1181. https://doi.org/10.1016/j.bpj.2013.07.038.
[19] G. Özbaykal, E. Wollrab, F. Simon, A. Vigouroux, B. Cordier, A. Aristov, T. Chaze, M. Matondo, S. van Teeffelen, The transpeptidase PBP2 governs initial localization and activity of the major cell-wall synthesis machinery in E. coli, eLife 9 (2020) e50629. https://doi.org/10.7554/eLife.50629.
[20] Y. Sun, S. Hürlimann, E. Garner, Growth rate is modulated by monitoring cell wall precursors in Bacillus subtilis, Nat. Microbiol. 8 (2023) 469–480. https://doi.org/10.1038/s41564-023-01329-7.
[21] P.J. Youngman, J.B. Perkins, R. Losick, Genetic transposition and insertional mutagenesis in Bacillus subtilis with Streptococcus faecalis transposon Tn917., Proc. Natl. Acad. Sci. U. S. A. 80 (1983) 2305–2309.
[22] C.R. Harwood, S.M. Cutting, Molecular biological methods for Bacillus, Wiley, 1990. https://scholar.google.com/scholar_lookup?title=Molecular+biological+methods+for+Bacillus&author=Harwood%2C+Colin+R.&publication_year=1990 (accessed July 19, 2022).
[23] K.L. Ellefsen, J.L. Dynes, I. Parker, Spinning-Spot Shadowless TIRF Microscopy, PLOS ONE 10 (2015) e0136055. https://doi.org/10.1371/journal.pone.0136055.
[24] M.G.L. Gustafsson, Surpassing the lateral resolution limit by a factor of two using structured illumination microscopy. SHORT COMMUNICATION, J. Microsc. 198 (2000) 82–87. https://doi.org/10.1046/j.1365-2818.2000.00710.x.
[25] F. Luisier, C. Vonesch, T. Blu, M. Unser, Fast interscale wavelet denoising of Poisson-corrupted images, Signal Process. 90 (2010) 415–427. https://doi.org/10.1016/j.sigpro.2009.07.009.
[26] P. Thevenaz, U.E. Ruttimann, M. Unser, A pyramid approach to subpixel registration based on intensity, IEEE Trans. Image Process. 7 (1998) 27–41. https://doi.org/10.1109/83.650848.
[27] J.C.M. Gebhardt, D.M. Suter, R. Roy, Z.W. Zhao, A.R. Chapman, S. Basu, T. Maniatis, X.S. Xie, Single-molecule imaging of transcription factor binding to DNA in live mammalian cells, Nat. Methods 10 (2013) 421–426. https://doi.org/10.1038/nmeth.2411.
[28] G. Cumming, R. Calin-Jageman, Introduction to the new statistics: Estimation, open science, and beyond, Routledge, 2016. https://books.google.com/books?hl=en&lr=&id=KR8xDQAAQBAJ&oi=fnd&pg=PP1&ots=1mrxLbuFZ2&sig=ubArAc2_GAOKQNfgt0fbXPM1z6A (accessed February 23, 2024).
[29] J. Ho, T. Tumkaya, S. Aryal, H. Choi, A. Claridge-Chang, Moving beyond P values: data analysis with estimation graphics, Nat. Methods 16 (2019) 565–566. https://doi.org/10.1038/s41592-019-0470-3.